

# Self-propulsion of an elliptic phoretic disk emitting solute uniformly

Guangpu Zhu<sup>1</sup> and Lailai Zhu<sup>1,\*</sup>

<sup>1</sup>*Department of Mechanical Engineering,  
National University of Singapore, 117575, Singapore*

arXiv:2304.06776v1 [physics.flu-dyn] 13 Apr 2023

# Abstract

Self-propulsion of chemically active droplet and phoretic disk has been widely studied; however, most research overlooks the influence of disk shape on swimming dynamics. Inspired by the experimentally observed prolate composite droplets and elliptic camphor disks, we employ simulations to investigate the phoretic dynamics of an elliptic disk that uniformly emits solutes in the creeping flow regime. By varying the disk's eccentricity  $e$  and the Péclet number  $Pe$ , we distinguish five disk behaviors: stationary, steady, orbiting, periodic, and chaotic. We perform a global linear stability analysis (LSA) to predict the onset of instability and the most unstable eigenmode when a stationary disk spontaneously transitions to steady self-propulsion. In addition to the LSA, we use an alternative approach to determine the perturbation growth rate, offering valuable insights into the competing roles of advection and diffusion. The steady motion features a transition from a puller-type to a neutral-type swimmer as  $Pe$  increases, which occurs as a bimodal concentration profile at the disk surface shifts to a polarized solute distribution, driven by convective solute transport. An elliptic disk achieves an orbiting motion through a chiral symmetry-breaking instability, wherein it repeatedly follows a circular path while simultaneously rotating. The swinging periodic motion, emerging from a steady motion via a supercritical Hopf bifurcation, is characterized by a wave-like trajectory. We uncover a transition from normal diffusion to superdiffusion as eccentricity  $e$  increases, corresponding to a random-walking circular disk and a ballistically swimming elliptic counterpart, respectively.

## I. INTRODUCTION

Synthetic micro-swimmers have attracted much attention owing to their promising potential in biomedical and bioengineering applications [70], e.g., detection and collection of metal ions [2], targeted controlled drug delivery [19, 76], and cancer-cells microsurgery [80]. Drawing inspiration from the propulsion strategies of microorganisms in nature, various bio-mimetic swimmers that propel in viscous fluids have been developed [20, 21, 38, 71]. Unlike their biological counterparts, these synthetic micro-swimmers are commonly powered by external forces or torques coming from the electric, optic, acoustic, or magnetic

---

\* [lailai.zhu@nus.edu.sg](mailto:lailai.zhu@nus.edu.sg)

fields [7, 10, 23, 38, 66], for example, a sperm-mimicking micro-swimmer with a flexible filament actuated magnetically [15]. Despite the rapid development of externally actuated micro-swimmers, some practical difficulties, such as miniaturization and manufacturing of moving parts for certain swimmers, have limited their applications in realistic scenarios [18, 33, 43, 64].

Unlike externally actuated swimmers, chemically active swimmers covert chemical energy stored internally or extracted from their surroundings into motion [53]. They can be broadly classified by whether their surface properties, e.g., surface activity and mobility, are anisotropic or isotropic. A classical anisotropic swimmer is the Janus colloid, e.g., the autophoretic Au-Pt Janus colloid [60]. The chemically patterned asymmetric colloid typically features two distinct compartments, each composed of a different material or bearing diverse functional groups [40], which enables asymmetric chemical reactions at the surface. The inherent asymmetry allows it to self-generate a concentration gradient, which drives a slip flow inducing net phoretic propulsion, as revealed by experimental [8, 16, 61], theoretical [6, 11, 22, 57] and numerical [37, 65, 69] studies. The Janus swimmer is typically micro-scale or even smaller, whose phoretic motion is Brownian [51]. Its self-propulsion requires a built-in asymmetry in the surface properties. This requirement presents a challenge to the controlled and reproducible manufacturing of Janus colloids, hence hindering their high-throughput production [52].

Chemically isotropic swimmers are much easier to manufacture compared to their anisotropic counterparts. A simple and typical representative of such swimmers is a chemically active droplet, e.g., a water droplet slowly dissolving in a surfactant-saturated oil phase [4], which have been extensively researched since their first experimental realization [30]. These active droplets are generally larger than the Janus microswimmers and have typical radii ranging from 10 to 100  $\mu\text{m}$ . Active droplets mainly consist of reacting droplets [35, 74, 78] and solubilizing droplets [26, 62, 68]. The former involve chemical reactions producing or changing surfactant molecules at their surface, while the latter feature a micellar dissolution into the surfactant-saturated ambient phase. In both instances, spatial modulation of the surface tension at the droplet interface may potentially induce Marangoni flows. Such droplets do not rely on built-in asymmetry like the Janus colloids, but instead attain self-propulsion via an instability spontaneously breaking the spatial symmetry. This instability arises from the nonlinear convective transport of solute species by fluid flow,

resulting from Marangoni and/or phoretic effects produced by local chemical gradients surrounding the droplet [54, 64]. Besides the active droplet, another class of chemically isotropic swimmers is camphor disks that surf at a liquid-air interface [56, 73, 79]. In this scenario, camphor molecules dissolved from the disk diffuse into the interface and further the subsurface liquid, and the Marangoni flows resulting from the solute gradient drive the disk to propel [5, 48]. Notably, the Marangoni flows generated by active droplets are solely at their surface, while those triggered by camphor disks are along the air-liquid interface and depend significantly on the depth of the subsurface liquid [48, 51].

Active droplets exhibit complex and tunable motion as a result of the nonlinear physico-chemical hydrodynamics [26, 42], characterized by the Péclet number  $Pe$  as the ratio of flow advection to solute diffusion. At low  $Pe$ , an isolated droplet remains stationary. Morozov & Michelin [55] identified the critical Péclet number for an undeformable droplet through a stability analysis, beyond which an unstable dipolar mode of hydrodynamics emerges, driving the spontaneous propulsion of the droplet. This critical  $Pe$  exactly matches that for a spherical phoretic particle [52]. In fact, the spherical particle can be considered as a droplet with infinite viscosity. Besides, the critical  $Pe$  determined for a two-dimensional (2D) undeformable droplet [42] is also consistent with that for a phoretic disk [27]. Near the critical  $Pe$ , the dipolar mode is the only unstable one [63, 67]. However, higher-order modes, e.g., the quadrupolar mode, becomes successively unstable with increasing  $Pe$ , leading to the possible coexistence of multiple unstable modes with different polar symmetries [26, 54]. Accordingly, the active droplet sequentially exhibits quasi-ballistic, unsteady curvilinear, and even chaotic motions [26, 39, 42, 75] as  $Pe$  grows. Analogous behaviors of 2D [27, 28] and three-dimensional (3D) isotropic phoretic particles have also been observed [9, 28, 34]. Besides an isolated unbounded droplet/particle, the effect of nearby boundaries [4, 12, 14, 31, 46, 64, 77], that of an ambient flow [13, 17, 83], and interaction among multiple droplets/particles [24, 32, 45, 49, 58, 81, 82] have been investigated.

Most of the active droplets observed in experiments were weakly deformed and remained spherical, one exception is the very recent work [25] reporting the self-propulsion of a prolate composite droplet along its minor axis. That oil droplet trapping two aqueous daughter droplets at the opposing poles of its major axis, suspended in an aqueous surfactant solution. The daughter droplets are submicellar, whereas the external aqueous phase is supramicellar. The micellar dissolution at the external oil-water interface induces a self-sustaining surface

tension gradient, driving the droplet motion. Compared to droplets, solid self-propelling swimmers relying on a similar symmetry-breaking mechanism exhibit greater flexibility in shape. Kitahata *et al.* [36] and [29] experimentally and theoretically investigated the spontaneous motion of an elliptic camphor disk at the air-liquid interface, and found that the disk swam along its minor axis resembling the swimming prolate droplet [25]. Motivated by these non-spherical phoretic swimmers with uniform chemical reactions at their surface, especially Kitahata *et al.* [36] and Hokmabad *et al.* [25], here, we theoretically and numerically explore, in the creeping flow regime, the instability-driven spontaneous propulsion of an elliptic phoretic disk that releases chemical species uniformly. We perform a global linear stability analysis to investigate the onset of instability, and direct numerical simulations to explore the swimming behavior of the phoretic disk.

This paper is organized as follows. We describe the problem setup, assumptions, and governing equations in Section II. The implementation for the global LSA is introduced in Section III, followed by Section IV demonstrating numerical and theoretical results. Finally, we conclude our observations and provide some discussion in Section V.

## II. PROBLEM SETUP, GOVERNING EQUATIONS AND METHODOLOGY

### A. Problem setup and governing equations

We consider a chemically active elliptic disk emitting or absorbing solute molecules uniformly in an incompressible Newtonian fluid of dynamic viscosity  $\bar{\eta}$  (see figure 1). From here on,  $\bar{\cdot}$  indicates dimensional variables unless otherwise mentioned. The semi-major and semi-minor axes of the disk are  $\bar{a}$  and  $\bar{b} \leq \bar{a}$ , respectively, and  $\bar{c}_f = \sqrt{\bar{a}^2 - \bar{b}^2}$  denotes the half of its focal length. Hence, the disk shape can be characterized by the eccentricity  $e = \bar{c}_f/\bar{a}$ , which recovers to 0 or approaches 1 as the disk becomes circular or needle-like. We choose the major axis of the disk to denote its orientation  $\mathbf{e}_s = \sin \theta \mathbf{e}_x + \cos \theta \mathbf{e}_y$ , which is characterized by its angular deviation from  $\mathbf{e}_y$ .

We now describe the phoretic dynamics of the elliptic disk and the associated governing equations. The disk's surface  $\Gamma_d$  uniformly emits or absorbs solutes with a constant rate  $\bar{A}$  (activity), hence,

$$\bar{D}\mathbf{n} \cdot \nabla \bar{c}|_{\Gamma_d} = -\bar{A}. \quad (1)$$

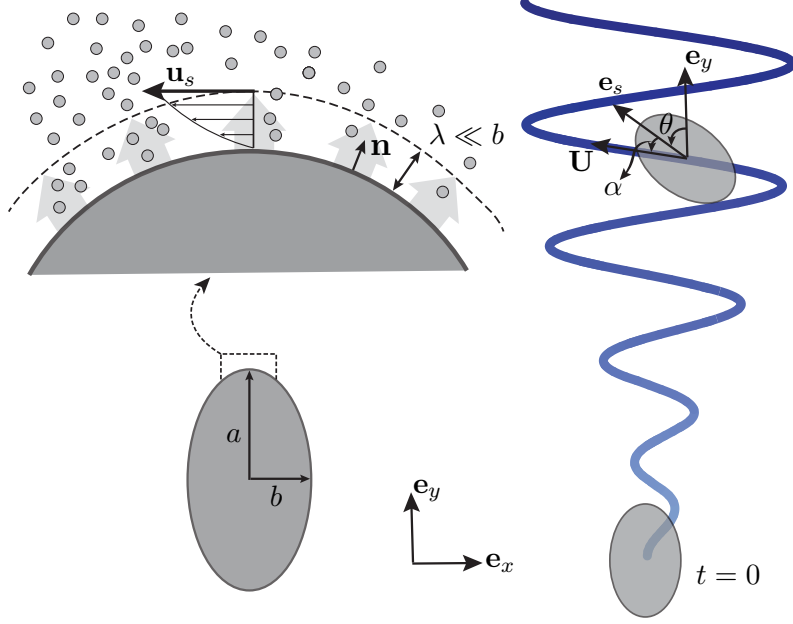


FIG. 1. Self-propulsion of an elliptic disk uniformly releasing chemical solutes in a Newtonian solvent.  $\mathbf{e}_{xy}$  denotes the laboratory frame. The disk moves along an undulatory path with a translational velocity of  $\mathbf{U}$  and the color of the path is coded by the time  $t$ . The disk orientation  $\mathbf{e}_s$  coinciding with its major axis deviates from  $\mathbf{e}_y$  and  $\mathbf{U}$  by angles  $\theta$  and  $\alpha$ , respectively. The inset shows the induced slip velocity  $\mathbf{u}_s$  by local solute gradients within a thin boundary layer of thickness  $\lambda \ll b$ .  $\mathbf{n}$  denotes the unit normal vector pointing away from the disk surface. All the variables here are dimensionless.

Here,  $\bar{c}$  is the solute concentration,  $\bar{D}$  denotes the molecular diffusivity of the solute, and  $\mathbf{n}$  is the unit outward normal at the surface. The solute interacts with the disk surface through a short-range potential and here we focus on the classical thin-interaction-layer limit  $\bar{\lambda} \ll \bar{b}$ , with  $\lambda$  the thickness of the interaction layer. Within this layer, the slip velocity along the disk surface induced by the local tangential solute gradients reads

$$\bar{\mathbf{u}}_s|_{\Gamma_d} = \bar{M} \nabla_s \bar{c}, \quad (2)$$

where  $\bar{\mathbf{u}}_s$  indicates the slip velocity,  $\nabla_s = (\mathbf{I} - \mathbf{nn}) \cdot \nabla$  is the surface gradient operator, and  $\bar{M}$  denotes the constant phoretic mobility. The signs of  $\bar{A}$  and  $\bar{M}$  depend on the physico-chemical properties of the disk. Positive or negative  $\bar{A}$  corresponds to the solute emission or absorption at the disk surface, respectively. Note that the spontaneous symmetry-breaking propulsion occurs only when  $\bar{A}\bar{M} > 0$  [27, 52], and the disk remains stable otherwise.

Without any loss of generality, this work will only consider positive  $\bar{A}$  and  $\bar{M}$ . Also, we assume that the inertia of both fluid and disk is negligible compared to the viscous force because the Reynolds number  $\text{Re}$  is typically small in the experiments [4, 24, 26, 47, 51, 62]. Hence, the fluid flow surrounding the disk can be described approximately by the Stokes equation.

In the following, we introduce the dimensionless governing equations. We choose  $\bar{A}\bar{M}/\bar{D}$ ,  $\bar{b}$ , and  $\bar{b}\bar{A}/\bar{D}$ , respectively, as the characteristic velocity  $\bar{\mathcal{V}}$ , length, and concentration for the nondimensionalization. All variables below are dimensionless unless otherwise specified. The dimensionless equations for the velocity  $\mathbf{u}$ , pressure  $p$ , and concentration  $c$  are

$$\nabla \cdot \boldsymbol{\sigma} = \mathbf{0}, \quad \nabla \cdot \mathbf{u} = 0, \quad (3)$$

$$\frac{\partial c}{\partial t} + \mathbf{u} \cdot \nabla c = \frac{1}{\text{Pe}} \Delta c, \quad (4)$$

where the Péclet number  $\text{Pe} = \bar{A}\bar{M}\bar{b}/\bar{D}^2$  measures the ratio of flow advection to solute diffusion and  $\boldsymbol{\sigma} = -p\mathbf{I} + \nabla\mathbf{u} + (\nabla\mathbf{u})^T$  is the hydrodynamic stress tensor. At the disk surface, the constant flux boundary condition (1) for the concentration reads

$$\mathbf{n} \cdot \nabla c|_{\Gamma_d} = -1. \quad (5)$$

We consider a circular fluid domain with a finite radius  $R$  and prescribe on its exterior  $\Gamma_o$

$$c|_{\Gamma_o} = 0. \quad (6)$$

It should be noted that equation (4) reduces to the Laplace equation when  $\text{Pe} \rightarrow 0$ , and the imposition of this Dirichlet boundary condition at the outer boundary at a finite distance ensures the well-posedness of our 2D model [27, 51]. Additionally, the domain radius  $R$  is known to affect the disk motion. Following Hu *et al.* [27] and Li [42], we set  $R = 200$ .

We perform numerical simulations in the frame co-moving with the disk center. Hence, the boundary conditions for the velocity at the disk surface  $\Gamma_d$  and the outer boundary  $\Gamma_o$  are

$$\mathbf{u}|_{\Gamma_d} = \mathbf{u}_s + \boldsymbol{\Omega} \times (\mathbf{x}_s - \mathbf{x}_c), \quad (7a)$$

$$\mathbf{u}|_{\Gamma_o} = -\mathbf{U}, \quad (7b)$$

where  $\mathbf{u}_s = \nabla_s c$  is the slip velocity at the disk surface,  $\mathbf{x}_s$  and  $\mathbf{x}_c$  denote the coordinates of a general point at the disk surface and the disk center, respectively. Here,  $\mathbf{U}$  and  $\boldsymbol{\Omega}$  denote

the translational and rotational velocities of the disk, respectively, which are determined by the force-free and torque-free conditions [41]

$$\mathbf{F} = \int \mathbf{n} \cdot \boldsymbol{\sigma} \, d\Gamma_d = \mathbf{0}, \quad (8a)$$

$$\mathbf{T} = \int (\mathbf{x}_s - \mathbf{x}_c) \times (\mathbf{n} \cdot \boldsymbol{\sigma}) \, d\Gamma_d = \mathbf{0}. \quad (8b)$$

Namely, the total force and torque exerted on the disk swimmer are zero. Equations (3)-(8) form the complete set of governing equations for an elliptic phoretic disk in the frame of co-moving with the disk.

## B. Numerical method

We numerically solve the governing equations, using a finite-element-method solver implemented in the commercial package COMSOL Multiphysics (I-Math, Singapore). We adopt the moving mesh technique to tackle the deformation of the fluid domain caused by disk rotation. Taylor-Hood and quadratic Lagrange elements are employed to discretize the flow field,  $(\mathbf{u}, p)$ , and the concentration  $c$ , respectively. The computational domain is discretized by approximately 85000 – 127000 triangular elements, and the mesh is locally refined near the disk. Our COMSOL implementations are extensively validated against several published datasets, as shown in Appendix A.

## III. GLOBAL LINEAR STABILITY ANALYSIS

Prior studies reveal that a chemically isotropic disk/droplet recovers a stationary state, termed base state, at a sufficiently low Pe. As Pe grows beyond a critical value, an instability arises, leading the disk/droplet to swim autonomously [27, 42, 55]. Our numerical results indicate that the elliptic disk here exhibits analogous behavior, hence we conduct a global LSA to examine the onset of global instability at a critical Péclet number  $\text{Pe}_c^{(1)}$ . The term ‘global instability’ here refers to the instability of a base state within a domain with either no homogeneous spatial direction or only one (in the case of a 3D domain). For the 2D domain under consideration, the global instability recovers to the local counterpart as the base state is homogeneous in one out of two spatial directions [59].

We first decompose the space- ( $\mathbf{x}$ ) and time-dependent state variables  $(c, \mathbf{u}, p)$  into the sum of a base state and a perturbation state as

$$c(\mathbf{x}, t) = c_b(\mathbf{x}) + c'(\mathbf{x}, t), \quad (9a)$$

$$\mathbf{u}(\mathbf{x}, t) = \mathbf{u}_b(\mathbf{x}) + \mathbf{u}'(\mathbf{x}, t), \quad (9b)$$

$$p(\mathbf{x}, t) = p_b(\mathbf{x}) + p'(\mathbf{x}, t), \quad (9c)$$

where the subscript  $b$  denotes base-state fields and the primed variables are infinitesimal perturbations. By substituting (9) into (3) and (4), and retaining linear terms, we obtain

$$\nabla \cdot \boldsymbol{\sigma}' = \mathbf{0}, \quad \nabla \cdot \mathbf{u}' = 0, \quad (10)$$

$$\frac{\partial c'}{\partial t} + \mathbf{u}_b \cdot \nabla c' + \mathbf{u}' \cdot \nabla c_b = \frac{1}{\text{Pe}} \Delta c'. \quad (11)$$

The perturbations are assumed to vary exponentially in time with a complex growth rate  $\sigma = \sigma_r + i\sigma_i$ , i.e.,

$$c'(\mathbf{x}, t) = \hat{c}(\mathbf{x}) e^{\sigma t}, \quad (12a)$$

$$\mathbf{u}'(\mathbf{x}, t) = \hat{\mathbf{u}}(\mathbf{x}) e^{\sigma t}, \quad (12b)$$

$$p'(\mathbf{x}, t) = \hat{p}(\mathbf{x}) e^{\sigma t}. \quad (12c)$$

Consequently, equations (10) and (11) can be reformulated to

$$\nabla \cdot \hat{\boldsymbol{\sigma}} = \mathbf{0}, \quad \nabla \cdot \hat{\mathbf{u}} = 0, \quad (13)$$

$$\sigma \hat{c} + \mathbf{u}_b \cdot \nabla \hat{c} + \hat{\mathbf{u}} \cdot \nabla c_b = \frac{1}{\text{Pe}} \Delta \hat{c}. \quad (14)$$

By expanding the translational and rotational velocities similarly, we arrive  $\mathbf{U} = \mathbf{U}_b + \hat{\mathbf{U}} e^{\sigma t}$  and  $\Omega = \Omega_b + \hat{\Omega} e^{\sigma t}$ . Substituting them with (9) into (5) to (7) enables us to derive the boundary conditions for  $\hat{c}$  and  $\hat{\mathbf{u}}$  at the disk surface and outer boundary

$$\mathbf{n} \cdot \nabla \hat{c}|_{\Gamma_p} = 0, \quad \hat{c}|_{\Gamma_o} = 0, \quad (15)$$

$$\hat{\mathbf{u}}|_{\Gamma_p} = \nabla_s \hat{c} + \hat{\Omega} \times (\mathbf{x}_s - \mathbf{x}_c), \quad \hat{\mathbf{u}}|_{\Gamma_o} = -\hat{\mathbf{U}}. \quad (16)$$

Note that  $\mathbf{U}_b$  and  $\Omega_b$  disappear in (16) corresponding to a stationary disk of the base state. The force-free and torque-free conditions still hold as

$$\hat{\mathbf{F}} = \int \mathbf{n} \cdot \hat{\boldsymbol{\sigma}} \, d\Gamma_p = \mathbf{0}, \quad (17a)$$

$$\hat{\mathbf{T}} = \int (\mathbf{x}_s - \mathbf{x}_c) \times (\mathbf{n} \cdot \hat{\boldsymbol{\sigma}}) \, d\Gamma_p = \mathbf{0}. \quad (17b)$$

Equations (13)-(17) define an eigenvalue problem. The stability of the base state is determined by the eigenvalue with the largest real part  $\sigma_r^0$ , namely the leading eigenvalue, and the corresponding perturbations  $(\hat{\mathbf{u}}, \hat{p}, \hat{c})^T$  are called leading eigenmodes. The base state is stable when  $\sigma_r^0 < 0$  but unstable when  $\sigma_r^0 > 0$ . The Péclet number at which  $\sigma_r^0 = 0$  is precisely the critical Péclet number  $\text{Pe}_c^{(1)}$  signifying the transition from a stationary state to steady propulsion. Unless stated otherwise, the eigenvalues mentioned below refer to the leading eigenvalues, and the superscript 0 is omitted for simplicity. We solve the eigenvalue problem with COMSOL using the eigenvalue solver ARPACK. The validation of our approach is demonstrated in Appendix A.

## IV. RESULTS

### A. Diverse behaviours of an elliptic phoretic disk

By increasing Péclet number  $\text{Pe}$ , we demonstrate the diverse  $\text{Pe}$ -dependent behaviors of a disk with the eccentricity  $e = 0.87$ . For a sufficiently small  $\text{Pe}$  below a critical value  $\text{Pe}_c^{(1)}$ , the disk undergoes transient rotation before recovering a stationary state. When  $\text{Pe}$  goes above  $\text{Pe}_c^{(1)}$ , e.g.,  $\text{Pe} = 0.4$ , the stationary state transits into the steady propulsion, in which the fore-aft symmetry in the concentration profile is broken (see Figure 2f), and the resultant concentration polarity induces a rectilinear motion with a constant swimming speed, as depicted in Figure 2(a). Further increasing  $\text{Pe}$  to 0.62, the directed motion loses its stability, leading to a secondary instability characterized by spontaneous chiral symmetry breaking. Consequently, the disk repeatedly executes a circular path, accompanied by its own clockwise rotation, as indicated in Figure 2(b). This regime featuring circular trajectory and self-rotation is called the orbiting regime. Hu *et al.* [27] and Li [42] observed analogous circular trajectories executed by circular swimmers without self-rotation. At  $\text{Pe} = 10$ , the elliptic disk favors a wave-like trajectory after a transient period of swimming straightforward (see Figure 2c). From the viewpoint of the frame co-moving with the disk center, the disk periodically swings like a pendulum (refer to Figure 2g). This swimming behavior is analogous to that exhibited by an active prolate double-core droplet, which moves along an undulatory trajectory [25]. Li [42] also reported that a high- $\text{Pe}$  active drop swims along a periodic zigzag trajectory. As  $\text{Pe}$  grows to 25, the elliptic disk surprisingly recovers to steady

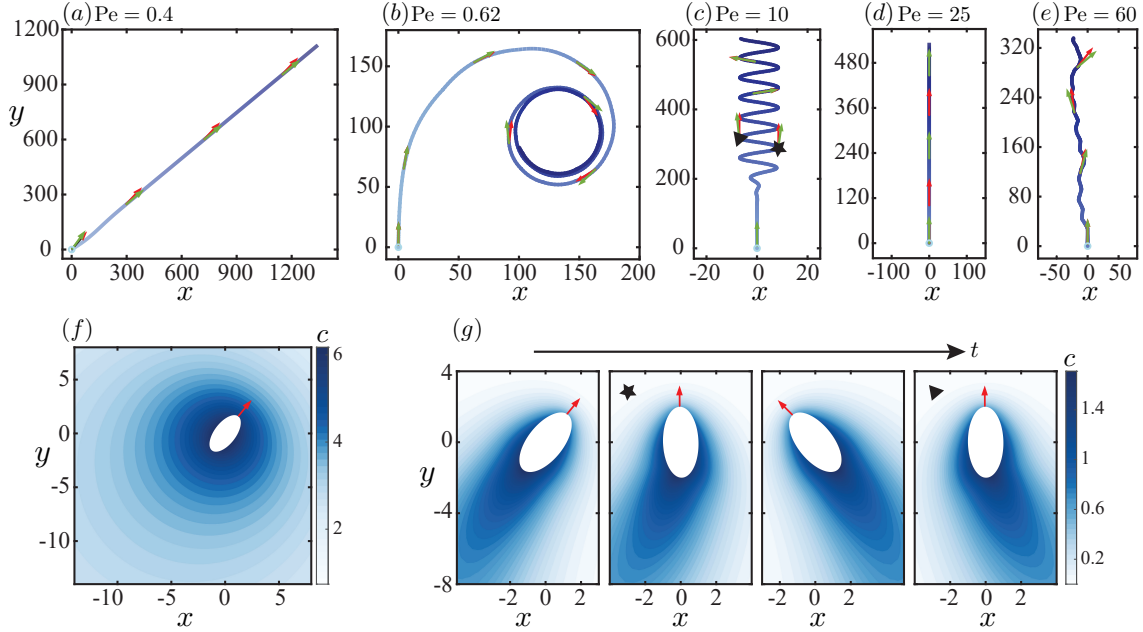


FIG. 2. An elliptic disk of eccentricity  $e = 0.87$  follows typical trajectories depending on  $Pe$ : (a) steady, (b) orbiting, (c) periodic, (d) steady, and (e) chaotic. The color of trajectories is coded by the time  $t$ . Green and red arrows denote the direction of the translational velocity  $\mathbf{U}$  and the disk orientation  $\mathbf{e}_s$ , respectively. (f) Polarized concentration distribution with respect to  $\mathbf{e}_s$  at  $Pe = 0.4$ . (g) Periodic pendulum-like swinging of the disk at  $Pe = 10$  in the frame co-moving with its center. The star and triangle symbols marked in (g) denote the two distinct moments when the disk reaches the peak and trough of its trajectory, respectively, as shown in (c).

propulsion, as illustrated in Figure 2(d). In correspondence, chiral symmetry recovers. Unlike the ballistic motion after rotation at low  $Pe$ , the disk here travels straight from the onset of instability without any rotation. The steady propulsion becomes unstable at a higher  $Pe$ , e.g.,  $Pe = 33$ , accordingly, the disk swims straightforward at an oscillating speed (see Figure 12 in Appendix B). Hu *et al.* [28] and Kailasham & Khair [34] identified the similar motion of an isotropic phoretic particle under the axisymmetric assumption. Figure 2(e) indicates that the disk enters into a chaotic regime characterized by an erratic trajectory at  $Pe = 60$ . In contrast to frequent intermittency and random walk occurring in the chaotic regime for a circular disk, as observed by Hu *et al.* [27], the change of velocity in both direction and magnitude experienced by the elliptic disk is not drastic, yielding a less chaotic trajectory.

Having observed distinct swimming behaviours of a disk with a specific eccentricity at varying  $Pe$ , we then systematically examine how the eccentricity  $e$  affects these  $Pe$ -dependent behaviours. The phase diagram in Figure 3 shows that shifts in  $Pe$ -dependent behaviours of an elliptic disk with  $e$  below 0.75, resemble those of a circular counterpart ( $e = 0$ ). The elliptic disk successively executes stationary, steady, periodic, and chaotic motion with increasing  $Pe$ . As  $e$  exceeds 0.75, the disk exhibits richer dynamics: the orbiting motion emerges with broken chiral symmetry. In fact, we have also explored the scenarios at  $e > 0.9$ , e.g.,  $e = 0.96$ , and observed that the swimming dynamics of the elliptic disk are almost dominated by orbiting and chaotic regimes (not shown here). These two regimes have been revealed in the current phase diagram, hence the characteristic locomotory modes can be well captured in the range of  $e$  considered.

We further discern from the phase diagram that the variation of  $e$  categorizes certain identified swimming patterns into two types. In the stationary or steady regime, the aforementioned observations indicate that the disk experiences transient rotation before recovering a stationary state or retaining a steady motion (see Figure 2). Nevertheless, these situations are only applicable at a higher  $e$ . When  $e < 0.75$ , the disk remains stationary or swims straight without any rotation. Besides, two types of periodic motions are depicted in the phase diagram: 1) a disk swings along a wavy trajectory (light-colored squares); 2) a disk swims straight at an oscillating swimming speed (dark-colored squares). The former and the latter are termed swinging and straight periodic motions, respectively.

## B. Spontaneous steady propulsion triggered by instability

Upon gaining a general understanding of the phase diagram, we then explore the detailed swimming dynamics within each regime. We first focus on the transition from the stationary to steady regime. The disk is stationary in the base state. As  $Pe$  exceeds  $Pe_c^{(1)}$ , an instability arises, and the disk sets into steady propulsion along its major axis. Here, we perform a global LSA, as introduced in Section III, to quantitatively identify  $Pe_c^{(1)}$  and its dependence on the disk shape.  $Pe_c^{(1)}$  predicted by the LSA monotonically decreases with  $e$ , as depicted by the solid line in the above phase diagram, implying that the ellipticity of the disk promotes its instability. Figure 4(a) depicts the concentration field  $\hat{c}$  of the global eigenmode at  $Pe_c^{(1)} = 0.43$  for  $e = 0.55$ . We see that the symmetry of the base concentration field  $\hat{c}$  is

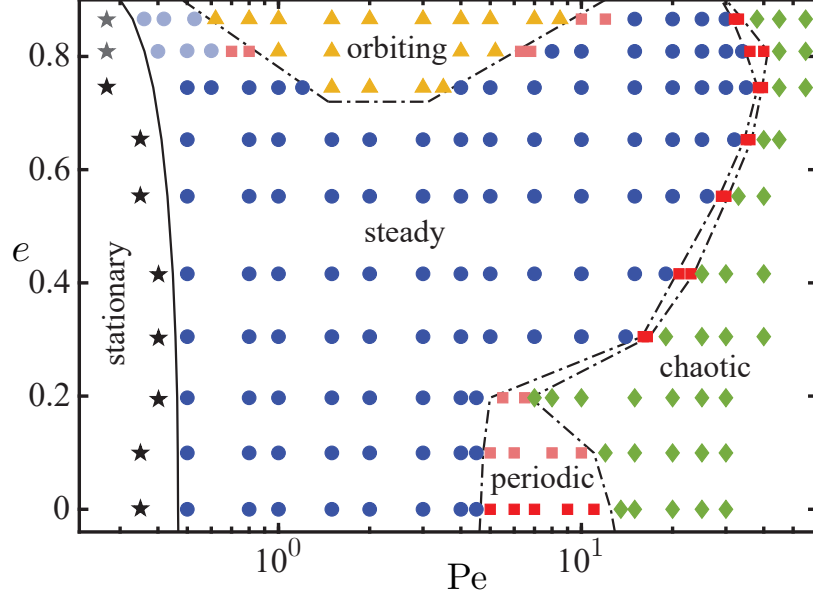


FIG. 3. Phase diagram characterizing the behaviors of an elliptic phoretic disk depending on its eccentricity  $e$  and the Péclet number  $Pe$ . It shows five regimes: stationary, steady, orbiting, periodic, and chaotic. The solid line denotes the LSA prediction.

broken in the direction of the major axis at  $Pe_c^{(1)}$ . The fore-aft asymmetric concentration distribution induces a downward slip flow, as shown by the flow field  $\hat{\mathbf{u}}$  of the eigenmode in figure 4(b), driving the steady motion of the disk along its major axis. In close proximity to  $Pe_c^{(1)}$ , the swimming speed  $U_{mg}$  is proportional to  $\sqrt{Pe - Pe_c^{(1)}}$  (see Figure 4c), implying that the instability occurs through a supercritical pitchfork bifurcation. This is parallel to the observation of Hu *et al.* [27] and Li [42].

We further probe the physical mechanism underlying the instability by adopting an approach resembling the energy budget analysis [1, 3]. By taking an inner product denoted by  $(\cdot, \cdot)$  of the equation (14) with  $\hat{c}$  in the  $L^2$  space, we arrive

$$(\sigma \hat{c}, \hat{c}) + (\hat{\mathbf{u}} \cdot \nabla c_b, \hat{c}) = \frac{1}{Pe} (\Delta \hat{c}, \hat{c}). \quad (18)$$

Using integration by parts, the divergence-free condition in (13), and the boundary condition (15), we derive

$$(\hat{\mathbf{u}} \cdot \nabla c_b, \hat{c}) = -(c_b, \hat{\mathbf{u}} \cdot \nabla \hat{c}), \quad (19a)$$

$$\frac{1}{Pe} (\Delta \hat{c}, \hat{c}) = -\frac{1}{Pe} \|\nabla \hat{c}\|^2, \quad (19b)$$

with  $\|\cdot\|$  denoting the  $L^2$ -norm. By substituting (19) into (18), we obtain

$$\sigma_e = \sigma_c + \sigma_d, \quad (20)$$

with

$$\sigma_c = \frac{(c_b, \hat{\mathbf{u}} \cdot \nabla \hat{c})}{(1, \hat{c}^2)}, \quad (21a)$$

$$\sigma_d = -\frac{\|\nabla \hat{c}\|^2}{(\text{Pe}, \hat{c}^2)}. \quad (21b)$$

Here, the growth rate  $\sigma_e$  is introduced in (20) to be distinguished from  $\sigma$  obtained by the LSA.  $\sigma_c$  and  $\sigma_d$  represent the contributions of advection and diffusion to  $\sigma_e$ , respectively. For a steady motion, the imaginary part of the growth rate vanishes, thus, the growth rate only has its real part, e.g.,  $\sigma = \sigma_r$ . Figure 4(c) shows that  $\sigma_e$  and  $\sigma$  lie on top of each other, giving us the confidence to analyze the dominant physical ingredient that drives the instability using (20). We naturally infer from (20) that  $\sigma_c$  is responsible for  $\sigma_e$  turning positive by realizing that  $\sigma_d$  is consistently negative, as confirmed by figure 4(c). Hence, as anticipated, advection drives the instability and diffusion dampens the perturbation, the balance between them dominates the phoretic dynamics of the elliptic disk: at small Pe, diffusion dominates and its homogenizing effect maintains a fore-aft symmetric solute distribution. As Pe grows beyond  $\text{Pe}_c^{(1)}$ , advection suppresses diffusion and amplifies the asymmetric solute disturbance. The slip flows triggered by the asymmetric concentration distribution drive the disk to swim spontaneously.

Next, we analyze the steady propulsion of the autophoretic disk. We show in figure 5(a) that the elliptic disk of  $e = 0.55$  swims as a puller attracting the fluid from its front and rear at  $\text{Pe} = 0.5$ . In contrast, it becomes a neutral-type swimmer at  $\text{Pe} = 1.5$ , as indicated in figure 5(b). In retrospect, Suda *et al.* [72] reported an analogous transition from a puller swimming straight into a pusher-type swimmer executing unsteady curvilinear motion when Pe increases. In that case, the droplet motion is triggered by the concentration gradient caused by a point source of surfactant at the surface. Besides, Li [42] observes that an active drop transits from a steady pusher to a mixed pusher-puller propelling unsteadily as Pe grows. For these droplet swimmers, the switching of their disturbance flow occurs as they go from steady to unsteady motion. Nevertheless, the disk swimmer here exhibits the puller-to-neutral transition without a shift in its swimming patterns. We further examine the flow field around a disk swimmer throughout the whole steady regime and summarize

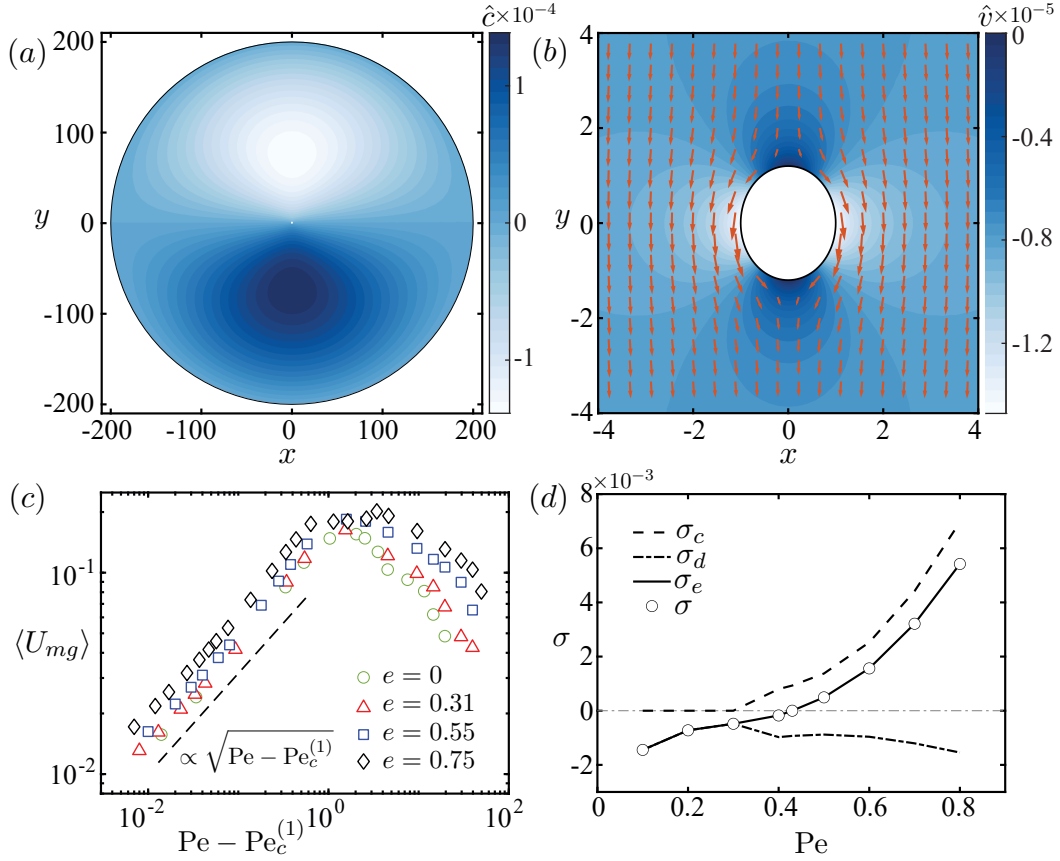


FIG. 4. Global eigenmodes at the critical Péclet number  $Pe_c^{(1)} = 0.43$  for an elliptic disk with  $e = 0.55$ . The eigenmode is characterized by (a) the perturbation concentration  $\hat{c}$ , and (b) the perturbation velocity  $\hat{\mathbf{u}}$  (red arrows) and its  $y$  component  $\hat{v}$  (color map). (c) Dependence of time-averaged disk speed  $\langle U_{mg} \rangle$  on  $Pe - Pe_c^{(1)}$  at varying  $e$ . In the vicinity of  $Pe_c^{(1)}$ ,  $\langle U_{mg} \rangle$  is proportional to  $\sqrt{Pe - Pe_c^{(1)}}$ . (d)  $Pe$ -dependent growth rate  $\sigma$  based on the LSA and that  $\sigma_e = \sigma_c + \sigma_d$  derived from the concentration perturbation equation (14). The latter comprises the contributions  $\sigma_c$  and  $\sigma_d$  from advection and diffusion, respectively.

these results in a phase diagram in figure 5(c). It is found that a circular ( $e = 0$ ) or nearly-circular disk can only be a neutral swimmer, and the puller-to-neutral transition emerges as  $e \geq 0.20$ . The critical Péclet number  $Pe_t$  signifying this transition depends monotonically on  $e$ , as indicated by the dashed line. When  $e > 0.65$ , the transition disappears and the disk solely swims as a puller. In fact, this peculiar transformation can be understood by examining the solute distribution at the disk surface, as discussed below. For visualization purpose, we normalize the concentration via  $\tilde{c} = \gamma(c_{max} - c) / (c_{max} - c_{min})$ , where  $c_{max}$  and

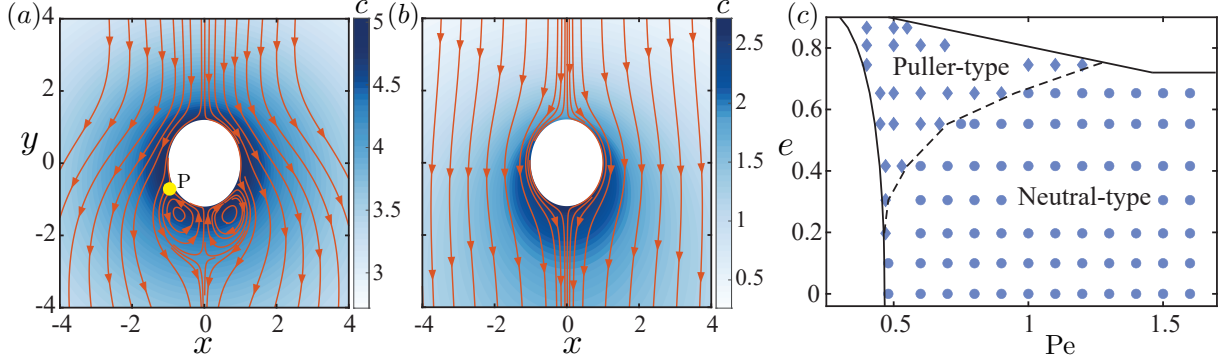


FIG. 5. (a) A puller-type steady swimmer at  $Pe = 0.5$  transitions to (b) a neutral-type counterpart at  $Pe = 1.5$ , where the eccentricity  $e$  is 0.55. The color maps indicate the distribution of  $c$ . The stagnation point  $P$  coincides with the peak of  $c$  at the disk surface. (c)  $Pe - e$  phase diagram shows puller-type and neutral-type steady swimmers demarcated by the dashed line. Solid lines separate regimes identified in figure 3.

$c_{min}$  denote the maximum and minimum concentrations at the disk surface, respectively. The coefficient  $\gamma$ , e.g.,  $\gamma = 0.5$ , restricts the normalized concentration  $\tilde{c}$  in the range of  $[0, \gamma]$ .

We demonstrate in figure 6(a) and (d) the bimodal distribution of normalized concentration caused by the curvature variation of the disk surface in the base state ( $Pe = 0.3$ ). The maximum normalized concentration  $\tilde{c}_{max}$  is located at the left vertex of the minor axis corresponding to  $\beta = 90^\circ$ , where  $\beta$  denotes the polar angle with respect to  $\mathbf{e}_s$ . Here, we consider only the left half of the disk ( $\beta \in [0, 180^\circ]$ ) for its symmetry. At  $Pe = 0.5$ , the base state loses stability and solutes are advected toward the disk's rear ( $\beta = 180^\circ$ ). Correspondingly, the position of  $c_{max}$  migrates rearward from  $\beta = 90^\circ$  to the stagnation point  $P$ , as depicted in figure 6(b). Considering that the slip velocity  $\mathbf{u}_s = \nabla_s c$  is directed from low to high concentration at the disk surface, the fluid is attracted from the front and rear of the elliptic disk to the stagnation position  $P$ , forming a puller-type swimmer (see figure 5a). As  $Pe$  increases to 1.5, the enhanced convective transport of solutes causes the shift from a bimodal to a polarized concentration profile with the peak concentration located at  $\beta = 180^\circ$  (see figure 6c). Correspondingly, the slip flow induced by the concentration gradient is driven from the front to the rear of the disk (see figure 6b), generating a prototypical neutral-type swimmer. We comment that as an elliptic disk swims steadily, a bimodal concentration profile at its surface yields a puller-type swimmer, while a polarized one leads to

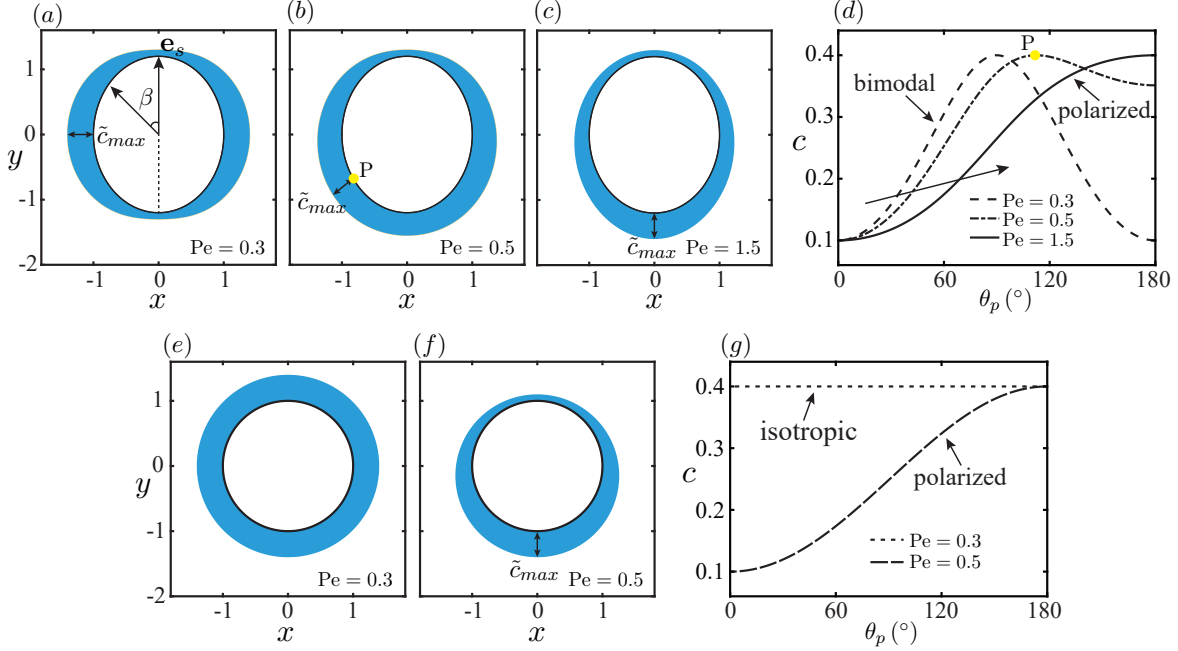


FIG. 6. Normalized concentration at the surface of a disk swimming steadily: (a)-(c) for an elliptic disk with  $e = 0.55$  at  $Pe = 0.3$ ,  $0.5$ , and  $1.5$ , respectively; (e)-(f) for a circular disk at  $Pe = 0.3$  and  $0.5$ , respectively.  $c_{max}$  denotes the peak concentration at the disk surface and  $\beta$  is the polar angle with respect to the disk orientation  $\mathbf{e}_s$ . The stagnation point  $P$  coincides with the location of  $\tilde{c}_{max}$  at  $Pe = 0.5$ . (d): transition from a bimodal to polarized concentration distribution at the surface of an elliptic disk by increasing  $Pe$ . (e): similar to (d) but for a circular disk with a transition from an isotropic solute distribution.

a neural-type counterpart. Different from the elliptic disk, a circular disk has an isotropic base distribution of the solute ( $Pe = 0.3$ ), as shown in figure 6(e) and (g). For an unstable base state at  $Pe = 1.5$ , solutes are advected rearward along the disk surface, leading to the direct transition from an isotropic to a polarized concentration profile. Hence, the circular disk behaves as a neutral swimmer solely.

### C. Chiral symmetry-breaking orbiting motion

Having observed the puller-neutral transition in the steady regime, we direct our focus on the chiral symmetry-breaking orbiting motion of the elliptic disk. Here, the disk approximately swims along a circular trajectory (see figure 2b) with the rotational velocity

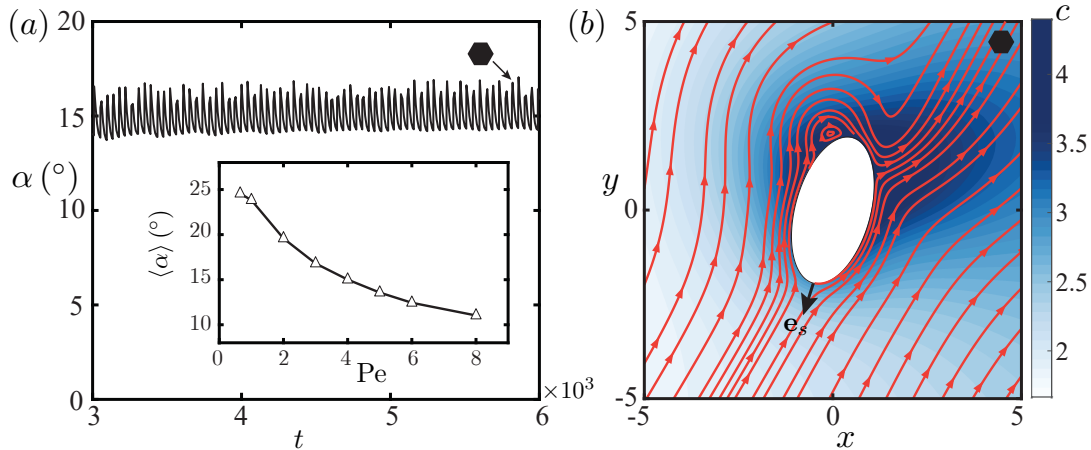


FIG. 7. (a) Time evolution of the angle  $\alpha$  between the translational velocity  $\mathbf{U}$  and the disk orientation  $\mathbf{e}_s$  as the elliptic disk with  $e = 0.87$  approximately follows a circular trajectory for  $Pe = 4$ . The inset shows the monotonic decrease of the time-averaged  $\alpha$  with  $Pe$ . (b) Solute distribution and streamlines at the instant indicated by a hexagon in (a).

$\Omega$  oscillating around a constant value. We find that the translational velocity  $\mathbf{U}$  (green arrow) deviates from  $\mathbf{e}_s$  (red arrow) by an angle  $\alpha$ . The evolution of  $\alpha$  resembles that of  $\Omega$  oscillating slightly around  $15^\circ$  for  $Pe = 4$ , as depicted in figure 7(a). In fact, the misalignment  $\mathbf{U}$  and  $\mathbf{e}_s$  can be rationalized by examining the solute distribution  $c(x, y)$  around the disk. Figure 7(b) illustrates  $c(x, y)$  and streamlines at the moment denoted by a hexagon in Figure 7(a). The left-right asymmetry of the solute distribution about  $\mathbf{e}_s$  gives rise to the asymmetric slip velocity, as reflected by the streamlines, hence causing the inconsistency in directions of  $\mathbf{U}$  and  $\mathbf{e}_s$ . Besides, we notice that three stagnation points near the rear of the disk in figure 7(b) gradually migrate toward the rear with increasing  $Pe$  in the orbiting regime (not shown here). Accordingly, the time-averaged  $\langle \alpha \rangle = \int_0^T \alpha dt / T$  within a time window  $T$  decreases monotonically with  $Pe$ , as shown in the inset of figure 7(a). Intuitively, we infer  $\mathbf{U}$  is aligned with  $\mathbf{e}_s$  ( $\alpha = 0$ ) as three stagnation points exactly coincide at the rear of the disk, and indeed they do as  $Pe$  grows beyond 14 where the disk executes a steady motion, e.g.,  $Pe = 25$  (streamlines and concentration distribution are analogous to Figure 5b).

The orbiting regime is characterized by the continuous rotation of an elliptic disk, which loses its chiral symmetry spontaneously. Conversely, a circular disk maintains this symmetry irrespective of the  $Pe$  value. In particular, for  $Pe \in [9, 13]$ , despite the asymmetric solute

distribution and streamlines resembling those in figure 7(b) occasionally, the circular disk only executes a meandering motion [27] without rotation. Ideally, a secondary stability analysis similar to the one performed above will help understand the mechanism for the shape-induced chiral symmetry breaking. This task is however technically challenging and will be pursued in the future.

Notably, experiments on active droplets in a Hele-Shaw cell showed that the droplet preferred to avoid the concentration trail emitted by itself at earlier times, termed a self-avoiding walk phenomenon [26]. The elliptic disk here does not avoid similarly but instead repeats its previous trajectory, as shown in figure 2(b). The difference can be rationalized by a scaling analysis. We estimate that the time  $\bar{t}_d$  required for the concentration to decay to zero is of the order of  $\bar{b}^2/\bar{D}$ . The disk moves with the speed  $U_{mg}\bar{\mathcal{V}}$ , hence the traveling time  $\bar{t}_p$  it takes to execute a circular trajectory of perimeter  $\bar{L}_p$  is  $\bar{L}_p/(U_{mg}\bar{\mathcal{V}})$  approximately. Recalling the definitions of  $\bar{\mathcal{V}}$  and Pe in Section II, we rewrite  $\bar{t}_p$  as  $\bar{L}_p\bar{b}/(U_{mg}\text{Pe}\bar{D})$ . The ratio between these two time scales is

$$\frac{\bar{t}_p}{\bar{t}_d} = \frac{\bar{L}_p/\bar{b}}{U_{mg}\text{Pe}}. \quad (22)$$

At a specific Pe, e.g., Pe = 4, in the orbiting regime,  $\bar{t}_p/\bar{t}_d \approx 87.2 \gg 1$ . This substantial ratio indicates that the disk swimmer can barely sense and thus avoid its own rapidly decaying chemical trace. In contrast, for a sufficiently larger Pe, we may observe the self-avoidance due to the significantly reduced travel time  $t_p$  [26, 28].

#### D. Periodic swinging

The orbiting motion typically transitions to periodic swinging (refer to figure 2c) as Pe increases, which will be analyzed below. Figure 8(a) illustrates that the time-evolving rotational velocity  $\Omega$  of the disk with  $e = 0.87$  at Pe = 12.5 is characterized by two phases. First,  $\Omega$  grows rapidly due to self-oscillation, and the dashed line connecting local peaks  $\Omega_{pk}$  of  $\Omega$  indicates an exponential growth of  $\Omega$  in time. This trend is confirmed by the linear relationship between  $\log \Omega_{pk}$  and  $t$  shown in the inset of figure 8(a). Second,  $\Omega$  saturates nonlinearly to a periodic state with a constant amplitude  $\Omega_{mg}$ . The sinusoidal-like variation of  $\Omega$  leads to a wave-like trajectory. We plot  $\Omega_{mg}^2$  as a function of Pe near the critical Pe  $\approx 13.5$  (star) in figure 8(b). The linear dependence of  $\Omega_{mg}^2$  on Pe implies that the steady

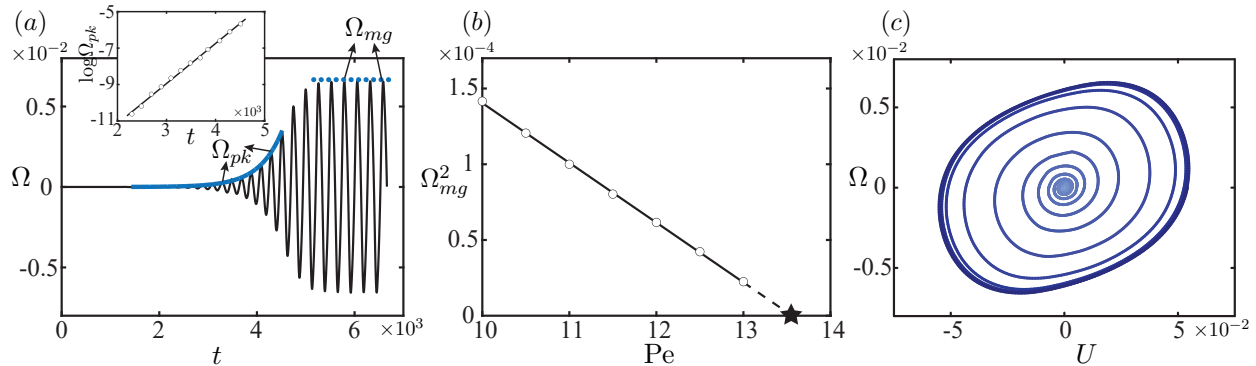


FIG. 8. (a) Time evolution of the rotational velocity  $\Omega$  of an elliptic disk with  $e = 0.87$  at  $Pe = 12.5$ . The dashed line denotes certain local peaks  $\Omega_{pk}$  of  $\Omega$ , and the inset shows the linear dependence of  $\log \Omega_{pk}$  on  $t$ . (b) Linear variation of  $\Omega_{mg}^2$  in  $Pe$  near the critical  $Pe \approx 13.5$  (star), where  $\Omega_{mg}$  denotes the constant amplitude of  $\Omega$  at  $t > 5400$ , as depicted by the dotted line in (a). The periodic motion recovers to steady propulsion as  $Pe$  grows beyond the critical value. (c) Phase portrait in the  $\Omega - U$  plane, with the color of the unstable spiral coded by  $t$ .

motion loses stability through a Hopf bifurcation. The critical  $Pe$  signifies the boundary between the periodic swinging and steady motion. We further present in Figure 8(c) the phase portrait in the  $\Omega - U$  plane, where the unstable spiral at the origin grows continuously to an elliptic stable limit circle, indicating the supercritical nature of the Hopf bifurcation. Notably, when  $e < 0.87$ , we observe a transition from steady to periodic swinging with increasing  $Pe$ , e.g.,  $e = 0.81$  (see Figure 3). The Hopf bifurcation still holds for the onset of instability that triggers this transition.

### E. Chaotic swimming dynamics

Finally, we analyze the chaotic motion of elliptic disks by examining their mean square displacement (MSD) and the velocity autocorrelation function (VAF). We calculate the MSD ( $\tau$ ) of a disk [50] that depends on a time lag  $\tau$  by

$$\text{MSD}(\tau) = \frac{1}{T - \tau} \int_0^{T-\tau} [\mathbf{r}(t + \tau) - \mathbf{r}(t)]^2, \quad (23)$$

where  $\mathbf{r}(t)$  denotes the time-dependent displacement of a disk relative to its original position. Clearly, combining a large time period  $T$  and  $\tau \ll T$  can improve the statistical confidence.

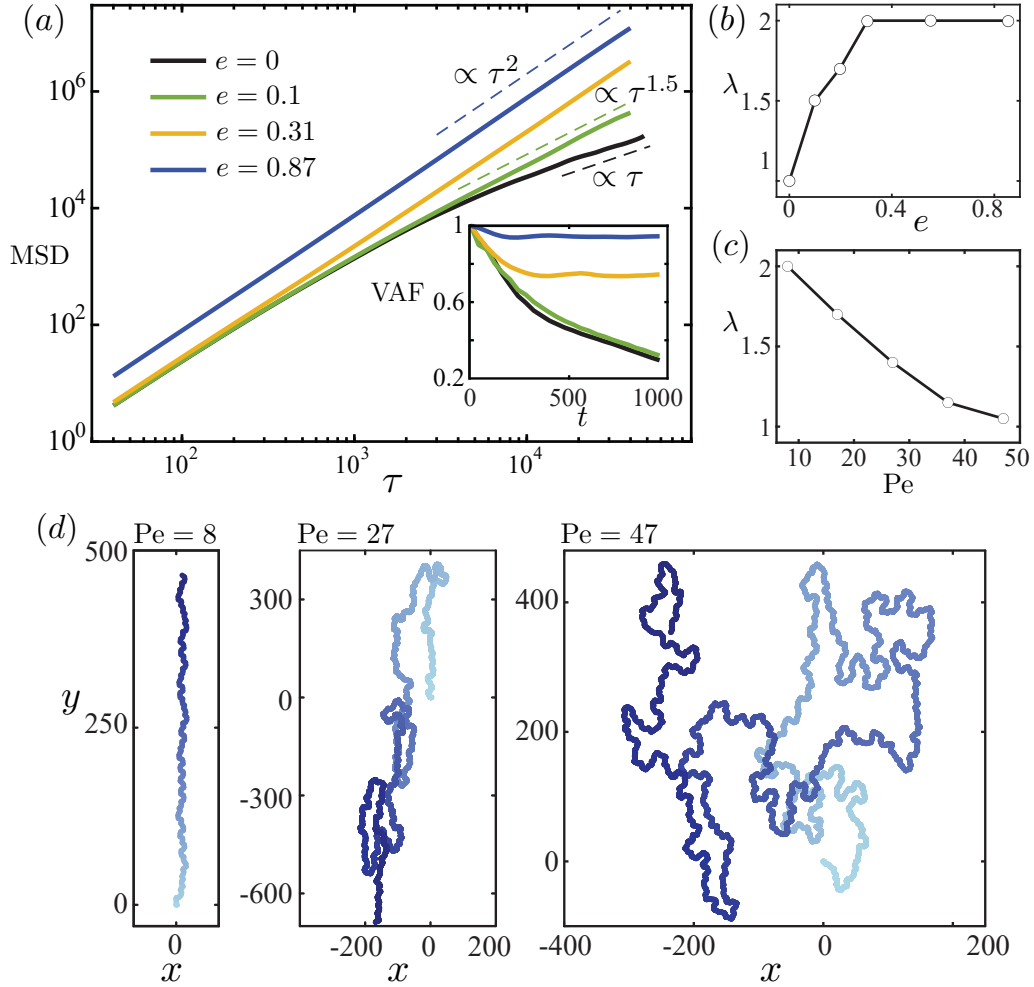


FIG. 9. (a) Mean square displacement (MSD) and velocity autocorrelation function (VAF) for disks with different shapes at  $Pe_c^{(2)} + 10$ , where  $Pe_c^{(2)}$  is the shape-dependent critical Péclet number corresponding to the onset of chaos. (b) The exponent  $\lambda$  of the power-law scaling  $MSD \propto \tau^\lambda$  versus  $e$ . (c) Monotonic dependence of  $\lambda$  on  $Pe$  for the disk of  $e = 0.2$ . (d) Chaotic trajectories (color-coded by  $t$ ) followed by an elliptic disk of  $e = 0.2$  at  $Pe = 8, 21$  and  $47$ , respectively.

We calculate VAF using

$$VAF(t) = \frac{1}{T} \int_0^T \frac{\mathbf{U}(t) \cdot \mathbf{U}(t + \Delta t)}{|\mathbf{U}(t)| |\mathbf{U}(t + \Delta t)|} dt, \quad (24)$$

where a sufficiently large  $T$  is used to attain statistical invariance [9].

We examine how the eccentricity  $e$  of a disk affects its chaotic motion. First, we determine the shape-dependent  $Pe_c^{(2)}(e)$  when chaos emerges. Then, we investigate the chaotic dynamics at  $Pe(e) = Pe_c^{(2)}(e) + 10$  above that threshold by a fixed offset, namely, 10 here. The corresponding MSD and VAF are depicted in figure 9(a). At early times, despite the

diversity in the disk shape, they all swim persistently resulting in the quadratically growing MSD in  $\tau$ . At long times, the disk shape considerably affects its phoretic movement, leading to a transition from a random-walking circular disk to a ballistically swimming elliptic counterpart. For the former, we reproduce perfectly its random walk behavior as reported by Hokmabad *et al.* [26], Hu *et al.* [27, 28], Lin *et al.* [44], which features the linear scaling  $\text{MSD} \propto \tau$  and the decorrelation in velocity  $\mathbf{U}$  due to the rapidly changing swimming direction (see the inset). As the eccentricity  $e$  increases to 0.1,  $\text{MSD} \propto \tau^{1.5}$ , reminiscent of the self-avoidance walk identified experimentally [26]. We wonder whether this growth scaling,  $\propto \tau^{1.5}$ , results from the self-avoidance walk. By utilizing the scaling analysis mentioned above, we compare the decay time of the chemical  $\bar{t}_d$  and the traveling time  $\bar{t}_p$  of the disk and find that  $\bar{t}_p/\bar{t}_d \approx 40.8 \gg 1$  (see Equation 22), precluding self-avoidance here. At  $e = 0.87$ , the MSD's quadratic growth over lag time implies that the elliptic disk approximately executes the ballistic motion, as confirmed by the trajectory shown in figure 2(e). Accordingly, the VAF is almost constant in time, indicating a correlation in velocity  $\mathbf{U}$ . It is worth noting that Hu *et al.* [28] and Morozov & Michelin [54] also found the quadratic variations of MSD for the chaotic swimming of a phoretic particle and an active droplet, respectively, under the axisymmetric assumption.

By probing further in figure 9 the exponent  $\lambda$  of power-law scaling  $\text{MSD} \propto \tau^\lambda$  at varying  $e$ , we notice that the normal diffusion ( $\lambda = 1$ ) transitions to superdiffusion ( $\lambda > 1$ ) as  $e$  increases. This observation demonstrates that the shape of a disk can significantly affect its diffusion behavior. In addition, we explore the effect of  $\text{Pe}$  on the chaotic motion of an elliptic disk, as depicted in figure 9(c). In contrast to the eccentricity  $e$ ,  $\lambda$  monotonically decreases with  $\text{Pe}$ , implying the transition from superdiffusion to normal diffusion. Accordingly, the elliptic disk undergoes a ballistic motion near  $\text{Pe}_c^{(2)}$  and swims randomly at a larger  $\text{Pe}$ , e.g.,  $\text{Pe} = 47$  (see figure 9d). An analogous dependence of  $\lambda$  on  $\text{Pe}$  for the chaotic motion of an axisymmetric spherical particle was also reported by Kailasham & Khair [34];

## V. CONCLUSIONS AND DISCUSSIONS

In this work, we numerically and theoretically investigate the swimming dynamics of an elliptic disk uniformly releasing solutes in the creeping flow regime. The disk with an eccentricity  $e < 0.75$  mimics a circular counterpart: it shows stationary, steady, periodic,

and chaotic behaviors dependent on  $Pe$ . When  $e > 0.75$ , the disk attains an orbiting motion via an instability spontaneously breaking the chiral symmetry.

By performing a global LSA, we theoretically predict the critical Péclet number  $Pe_c^{(1)}$  above which a stationary disk becomes a steady swimmer spontaneously triggered by instability. The ellipticity of the disk is found to promote this instability. Besides the LSA, we calculate the growth rate of perturbation via a method akin to energy budget analysis. The results agree with the LSA predictions and provide new insight into the competing roles of advection and diffusion.

We observe that the transition from a puller-type to a neutral-type steady disk swimmer is induced by a stronger rearward advection of solute due to growing  $Pe$ . Accordingly, a bimodal concentration profile corresponding to a puller-type swimmer becomes a polarized profile leading to a neutral-type swimmer. The orbiting disk repeatedly swims along a circular trajectory while simultaneously rotating.

Two distinct types of periodic motions are identified: swinging and straight periodic motions. The former develops from a steady motion through a supercritical Hopf bifurcation and features a wave-like trajectory. The latter is characterized by a rectilinear motion with an oscillating swimming speed. Finally, the effects of the disk shape and  $Pe$  on the chaotic motion are examined. We uncover a shift from normal diffusion to superdiffusion with growing eccentricity  $e$ : the former and latter correspond to a random-walking circular disk and a ballistically swimming elliptic counterpart, respectively. The influence of  $Pe$  on the disk's diffusion behavior stands in contrast to that of  $e$ .

It is important to note that both the elliptic camphor disk [36] and the prolate composite droplet [25] observed in laboratory studies demonstrate self-propulsion along their minor axes. In contrast, the elliptic phoretic disk in this work swims steadily along its major axis. The differences in these cases may be due to the failure of 2D simulations to capture the complex 3D physicochemical hydrodynamics present in experiments. Specifically, a swimming camphor disk is driven by Marangoni flow at the air-liquid interface and the resulting 3D subsurface flow, while the prolate droplet self-propels within a Hele-Shaw cell. We are planning 3D studies to address these discrepancies.

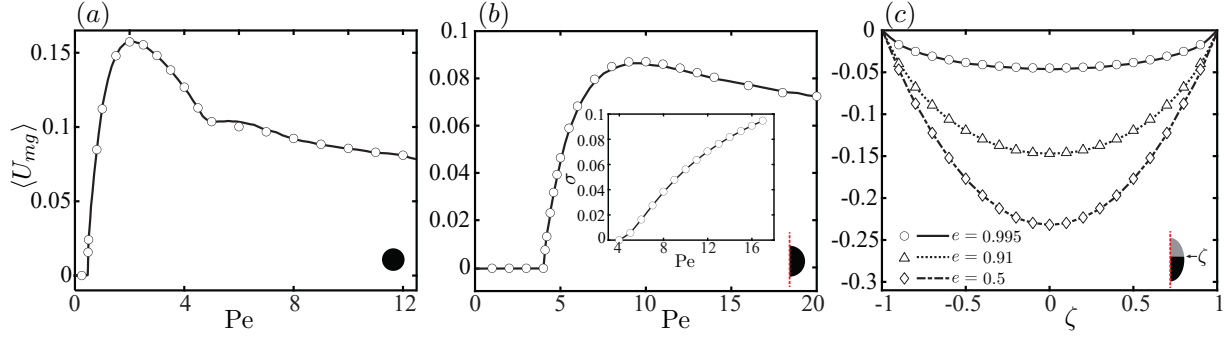


FIG. 10. Validation of our numerical implementation against published works. The numerical and published data are represented by markers and lines, respectively. (a) Swimming speed of an isotropic autophoretic disk in a circular domain of radius  $R = 200$  for varying  $Pe$ , benchmarked by [27]. Note that the time-averaged swimming speed  $\langle U_{mg} \rangle = \int_0^T U_{mg} dt$  within a time period  $T$  recovers  $U_{mg}$  for steady propulsion. (b) Swimming speed of an autophoretic spherical particle versus  $Pe$  computed in an axisymmetric configuration, in comparison to Michelin *et al.* [52]; the inset shows the growth rate  $\sigma$  of the unstable eigenmode versus  $Pe$ . (c) Swimming velocity of a spheroidal Janus particle as a function of  $\zeta$ , validated against Popescu *et al.* [65].  $\zeta$  denotes the height of the border dividing the particle into active and inert (marked in grey) compartments, with  $\zeta = 0$  corresponding to the particle center. The eccentricity  $e$  of the spheroid recovers to zero for a spherical particle.

### Appendix A: Validation of numerical implementations

We show the validation of our COMSOL implementations for the numerical simulation (Equations (3)-(8)) and stability analysis (Equations (13)-(17)). First, we study the inertialess self-propulsion of an isotropic autophoretic disk in a circular domain of radius  $R = 200$ . This setup has been investigated by Hu *et al.* [27] combining a stability analysis and simulations based on a spectral method. The disk transits to a steady swimmer from its stationary state at the first threshold  $Pe \approx 0.466$ . Increasing  $Pe$ , the swimmer becomes unstable at the second critical condition  $Pe \approx 4.65$ , moving in a meandering manner. Our numerical data shown in Figure 10(a) exactly recovers the reported  $Pe$ -dependent swimming speed and two critical  $Pe$  values. Besides the 2D case, we examine the spontaneous motion of an axisymmetric isotropic particle in an unbounded domain. In this case, instability occurs at  $Pe = 4$  as predicted by Michelin *et al.* [52]. Our data on swimming speed agrees well with

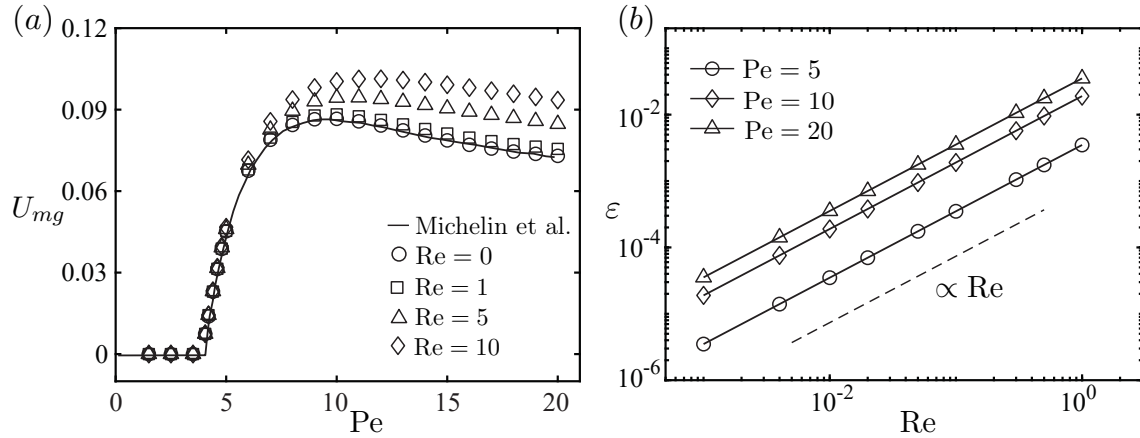


FIG. 11. (a) Swimming speed  $U_{mg}$  of an isotropic phoretic particle versus  $Pe$  when  $Re$  varies, which is calculated in an axisymmetric setup. Our numerical data are compared with that of Michelin *et al.* [52] at  $Re = 0$ . (b) Inertia enhances the swimming speed, characterized by the linear relation between the relative enhancement  $\varepsilon = [U_{mg}(Re, Pe) - U_{mg}(Re = 0, Pe)] / U_{mg}(Re = 0, Pe)$  and  $Re$ .

the numerical results therein, as depicted in Figure 10(b). Also, its inset shows that the present LSA recovers the threshold  $Pe = 4$  and the eigenvalues depending on  $Pe$ . As a side product, we probe the effect of inertia  $Re$  on this scenario. The inertial effect systematically enhances the swimming speed, becoming pronounced when  $Re > 1$  (see Figure 11a). The inertia-induced relative enhancement of the swimming speed  $\varepsilon$  in Figure 11(b) is observed to linearly scale with  $Re$  in this weak inertia regime, which deserves further theoretical underpinning.

Finally, we examine the ability of our implementation in handling non-spherical phoretic swimmers. We focus on a spheroidal Janus colloid consisting of active and inert compartments. Its propulsion depends on its eccentricity  $e$  and  $\zeta$ , where  $\zeta$  denotes the height of the border separating the two compartments. The obtained swimming speed agrees well with the reference solutions over a wide range of  $e$  and  $\zeta$  [65], as shown in Figure 10(c).

## Appendix B: Periodic motion of an elliptic phoretic disk

We identify two types of periodic motion: the first showcases a wave-like trajectory caused by the periodic rotation of the elliptic disk (see Figure 2g); the second corresponds to unidirectional rectilinear motion with a time-periodic swimming speed, as shown in Figure

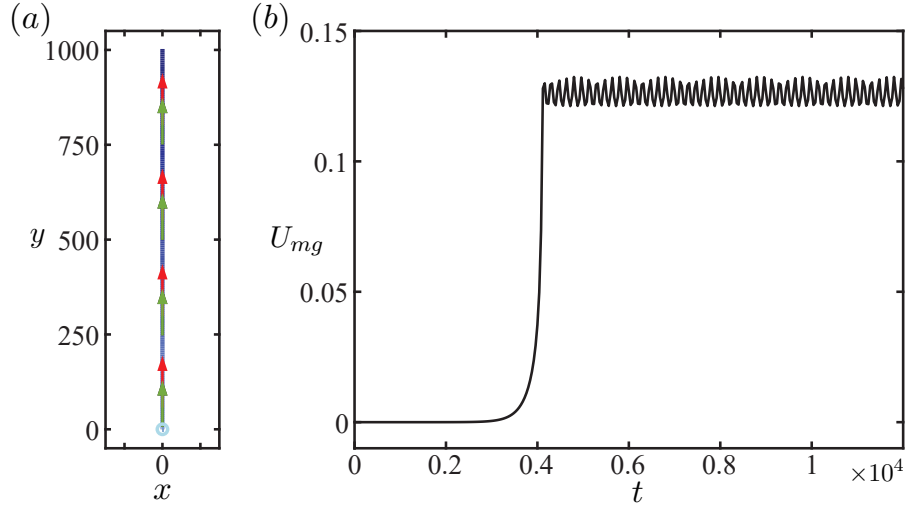


FIG. 12. Straight periodic motion of an elliptic disk with  $e = 0.87$  at  $Pe = 33$ . (a) Straight trajectory color-coded by time  $t$ . The swimming direction  $\mathbf{e}_s$  (red arrow) coincides with the translational velocity  $\mathbf{U}$  (green arrow). (b) Time evolution of the swimming speed  $U_{mg}$ .

12.

## ACKNOWLEDGMENTS

We thank Qianhong Yang for helpful discussions and Wei-Fan Hu for generously sharing the data utilized in the validation. L.Z. thanks Singapore Ministry of Education Academic Research Fund Tier 2 (MOE-T2EP50221-0012 & MOE-T2EP50122-0015) and Tier 1 (A-8000197-01-00) grants, and the Paris-NUS joint research grant (ANR-18-IDEX-0001 & A-0009528-01-00). Some computation of the work was performed on resources of the National Supercomputing Centre, Singapore.

- 
- [1] ABUBAKAR, HA & MATAR, OK 2022 Linear stability analysis of taylor bubble motion in downward flowing liquids in vertical tubes. *J. Fluid Mech.* **941**, A2.
- [2] BAN, TAKAHIKO, SUGIYAMA, MICHIAKI, NAGATSU, YUICHIRO & TOKUYAMA, HIDEAKI 2018 Motion-based detection of lanthanides (III) using self-propelled droplets. *J. Phys. Chem. B* **122** (46), 10647–10651.

- [3] BENDIKSEN, KJELL H 1985 On the motion of long bubbles in vertical tubes. *Int. J. Multiphas. Flow* **11** (6), 797–812.
- [4] DE BLOIS, CHARLOTTE, REYSSAT, MATHILDE, MICHELIN, SÉBASTIEN & DAUCHOT, OLIVIER 2019 Flow field around a confined active droplet. *Phys. Rev. Fluids* **4** (5), 054001.
- [5] BONIFACE, DOLACHAI, COTTIN-BIZONNE, CÉCILE, DETCHEVERRY, FRANÇOIS & YBERT, CHRISTOPHE 2021 Role of marangoni forces in the velocity of symmetric interfacial swimmers. *Phys. Rev. Fluids* **6** (10), 104006.
- [6] BRADY, JOHN F 2011 Particle motion driven by solute gradients with application to autonomous motion: continuum and colloidal perspectives. *J. Fluid Mech.* **667**, 216–259.
- [7] BUNEA, ADA-IOANA & GLÜCKSTAD, JESPER 2019 Strategies for optical trapping in biological samples: Aiming at microrobotic surgeons. *Laser Photonics Rev.* **13** (4), 1800227.
- [8] CAMPBELL, ANDREW I, EBBENS, STEPHEN J, ILLIEN, PIERRE & GOLESTANIAN, RAMIN 2019 Experimental observation of flow fields around active Janus spheres. *Nat. Commun.* **10** (1), 1–8.
- [9] CHEN, YIBO, CHONG, KAI LEONG, LIU, LUOQIN, VERZICCO, ROBERTO & LOHSE, DETLEF 2021 Instabilities driven by diffusiophoretic flow on catalytic surfaces. *J. Fluid Mech.* **919**.
- [10] CHEN, YUFENG, ZHAO, HUICHAN, MAO, JIE, CHIRARATTANANON, PAKPONG, HELBLING, E FARRELL, HYUN, NAK-SEUNG PATRICK, CLARKE, DAVID R & WOOD, ROBERT J 2019 Controlled flight of a microrobot powered by soft artificial muscles. *Nature* **575** (7782), 324–329.
- [11] DATT, CHARU, NATALE, GIOVANNIANTONIO, HATZIKIRIAKOS, SAVVAS G & ELFRING, GWYNN J 2017 An active particle in a complex fluid. *J. Fluid Mech.* **823**, 675–688.
- [12] DESAI, NIKHIL & MICHELIN, SÉBASTIEN 2021 Instability and self-propulsion of active droplets along a wall. *Phys. Rev. Fluids* **6** (11), 114103.
- [13] DEY, RANABIR, BUNESS, CAROLA M, HOKMABAD, BABAK VAJDI, JIN, CHENYU & MAASS, CORINNA C 2021 Oscillatory rheotaxis of active droplets in microchannels. *arXiv preprint arXiv:2106.10222* .
- [14] DEY, RANABIR, BUNESS, CAROLA M, HOKMABAD, BABAK VAJDI, JIN, CHENYU & MAASS, CORINNA C 2022 Oscillatory rheotaxis of artificial swimmers in microchannels. *Nat. Commun.* **13** (1), 1–10.
- [15] DREYFUS, RÉMI, BAUDRY, JEAN, ROPER, MARCUS L, FERMIGIER, MARC, STONE,

- HOWARD A & BIBETTE, JÉRÔME 2005 Microscopic artificial swimmers. *Nature* **437** (7060), 862–865.
- [16] DUAN, WENTAO, WANG, WEI, DAS, SAMBEETA, YADAV, VINITA, MALLOUK, THOMAS E & SEN, AYUSMAN 2015 Synthetic nano-and micromachines in analytical chemistry: sensing, migration, capture, delivery, and separation. *Annu Rev Anal Chem* **8**, 311–333.
- [17] DWIVEDI, PRATEEK, SHRIVASTAVA, ATISHAY, PILLAI, DIPIN & MANGAL, RAHUL 2021 Rheotaxis of active droplets. *Phys. Fluids* **33** (8), 082108.
- [18] EBRAHIMI, NAFISEH, BI, CHENGHAO, CAPPELLERI, DAVID J, CIUTI, GASTONE, CONN, ANDREW T, FAIVRE, DAMIEN, HABIBI, NEDA, HOŠOVSKÝ, ALEXANDER, IACOVACCI, VERONICA, KHALIL, ISLAM SM & OTHERS 2021 Magnetic actuation methods in bio/soft robotics. *Adv. Funct. Mater.* **31** (11), 2005137.
- [19] FU, JINGLIN & YAN, HAO 2012 Controlled drug release by a nanorobot. *Nat. Biotechnol.* **30** (5), 407–408.
- [20] GAO, WEI, SATTAYASAMITSATHIT, SIRILAK, MANESH, KALAYIL MANIAN, WEIHS, DANIEL & WANG, JOSEPH 2010 Magnetically powered flexible metal nanowire motors. *J. Am. Chem. Soc.* **132** (41), 14403–14405.
- [21] GHOSH, AMBARISH & FISCHER, PEER 2009 Controlled propulsion of artificial magnetic nanostructured propellers. *Nano Lett.* **9** (6), 2243–2245.
- [22] GOLESTANIAN, RAMIN, LIVERPOOL, TB & AJDARI, A 2007 Designing phoretic micro-and nano-swimmers. *New J. Phys.* **9** (5), 126.
- [23] HAN, E., ZHU, L., SHAEVITZ, J. W. & STONE, H. A. 2021 Low-Reynolds-number, biflagellated quince swimmers with multiple forms of motion. *Proc. Natl. Acad. Sci. USA* **118** (29), e2022000118.
- [24] HOKMABAD, BABAK VAJDI, AGUDO-CANALEJO, JAIME, SAHA, SUROPRIYA, GOLESTANIAN, RAMIN & MAASS, CORINNA C 2022 Chemotactic self-caging in active emulsions. *Proc. Natl. Acad. Sci. USA* **119** (24), e2122269119.
- [25] HOKMABAD, BABAK VAJDI, BALDWIN, KYLE A, KRÜGER, CARSTEN, BAHR, CHRISTIAN & MAASS, CORINNA C 2019 Topological stabilization and dynamics of self-propelling nematic shells. *Phys. Rev. Lett.* **123** (17), 178003.
- [26] HOKMABAD, BABAK VAJDI, DEY, RANABIR, JALAAL, MAZIYAR, MOHANTY, DEVADITYA, ALMUKAMBETOVA, MADINA, BALDWIN, KYLE A, LOHSE, DETLEF & MAASS, CORINNA C

- 2021 Emergence of bimodal motility in active droplets. *Phys. Rev. X* **11** (1), 011043.
- [27] HU, WEI-FAN, LIN, TE-SHENG, RAFAI, SALIMA & MISBAH, CHAOUQI 2019 Chaotic swimming of phoretic particles. *Phys. Rev. Lett.* **123** (23), 238004.
- [28] HU, WEI-FAN, LIN, TE-SHENG, RAFAI, SALIMA & MISBAH, CHAOUQI 2022 Spontaneous locomotion of phoretic particles in three dimensions. *Phys. Rev. Fluids* **7** (3), 034003.
- [29] IIDA, KEITA, KITAHATA, HIROYUKI & NAGAYAMA, MASAHARU 2014 Theoretical study on the translation and rotation of an elliptic camphor particle. *Phys. D: Nonlinear Phenom.* **272**, 39–50.
- [30] IZRI, ZIANE, VAN DER LINDEN, MARJOLEIN N, MICHELIN, SÉBASTIEN & DAUCHOT, OLIVIER 2014 Self-propulsion of pure water droplets by spontaneous marangoni-stress-driven motion. *Phys. Rev. Lett.* **113** (24), 248302.
- [31] JIN, CHENYU, HOKMABAD, BABAK V, BALDWIN, KYLE A & MAASS, CORINNA C 2018 Chemotactic droplet swimmers in complex geometries. *J. Phys.: Condens. Matter* **30** (5), 054003.
- [32] JIN, CHENYU, KRÜGER, CARSTEN & MAASS, CORINNA C 2017 Chemotaxis and autochemotaxis of self-propelling droplet swimmers. *Proc. Natl. Acad. Sci. USA* **114** (20), 5089–5094.
- [33] JOH, HYUNGMOK & FAN, DONGLEI EMMA 2021 Materials and schemes of multimodal reconfigurable micro/nanomachines and robots: Review and perspective. *Adv. Mater.* **33** (39), 2101965.
- [34] KAILASHAM, R & KHAIR, ADITYA S 2022 Dynamics of forced and unforced autophoretic particles. *J. Fluid Mech.* **948**, A41.
- [35] KASUO, YUI, KITAHATA, HIROYUKI, KOYANO, YUKI, TAKINOUE, MASAHIRO, ASAKURA, KOUICHI & BANNO, TAISUKE 2019 Start of micrometer-sized oil droplet motion through generation of surfactants. *Langmuir* **35** (41), 13351–13355.
- [36] KITAHATA, HIROYUKI, IIDA, KEITA & NAGAYAMA, MASAHARU 2013 Spontaneous motion of an elliptic camphor particle. *Phys. Rev. E* **87** (1), 010901.
- [37] KOHL, RYAN, CORONA, EDUARDO, CHERUVU, VANI & VEERAPANENI, SHRAVAN 2021 Fast and accurate solvers for simulating janus particle suspensions in stokes flow. *arXiv preprint arXiv:2104.14068* .
- [38] KOLEOSO, MUSTAPHIS, FENG, XUE, XUE, YUXIANG, LI, QUAN, MUNSHI, TASNIM & CHEN, XIANFENG 2020 Micro/nanoscale magnetic robots for biomedical applications. *Mater*

- 8, 100085.
- [39] KRÜGER, CARSTEN, KLÖS, GUNNAR, BAHR, CHRISTIAN & MAASS, CORINNA C 2016 Curling liquid crystal microswimmers: A cascade of spontaneous symmetry breaking. *Phys. Rev. Lett.* **117** (4), 048003.
- [40] LATTUADA, MARCO & HATTON, T ALAN 2011 Synthesis, properties and applications of Janus nanoparticles. *Nano Today* **6** (3), 286–308.
- [41] LAUGA, ERIC & POWERS, THOMAS R 2009 The hydrodynamics of swimming microorganisms. *Rep. Prog. Phys.* **72** (9), 096601.
- [42] LI, GAOJIN 2022 Swimming dynamics of a self-propelled droplet. *J. Fluid Mech.* **934**.
- [43] LI, MENG, PAL, ANIKET, AGHAKHANI, AMIRREZA, PENA-FRANCESCH, ABDON & SITTI, METIN 2022 Soft actuators for real-world applications. *Nat. Rev. Mater.* **7** (3), 235–249.
- [44] LIN, TE-SHENG, HU, WEI-FAN & MISBAH, CHAOUQI 2020 A direct poisson solver in spherical geometry with an application to diffusiophoretic problems. *J. Comput. Phys.* **409**, 109362.
- [45] LIPPERA, KEVIN, BENZAQUEN, MICHAEL & MICHELIN, SÉBASTIEN 2020 Bouncing, chasing, or pausing: Asymmetric collisions of active droplets. *Phys. Rev. Fluids* **5** (3), 032201.
- [46] LIPPERA, KEVIN, MOROZOV, MATVEY, BENZAQUEN, MICHAEL & MICHELIN, SÉBASTIEN 2020 Collisions and rebounds of chemically active droplets. *J. Fluid Mech.* **886**.
- [47] MAASS, CORINNA C, KRÜGER, CARSTEN, HERMINGHAUS, STEPHAN & BAHR, CHRISTIAN 2016 Swimming droplets. *Annu. Rev. Condens. Matter Phys.* **7**, 171–193.
- [48] MATSUDA, YUI, SUEMATSU, NOBUHIKO J, KITAHATA, HIROYUKI, IKURA, YUMIHIKO S & NAKATA, SATOSHI 2016 Acceleration or deceleration of self-motion by the marangoni effect. *Chem. Phys. Lett.* **654**, 92–96.
- [49] MEREDITH, CALEB H, MOERMAN, PEPIJN G, GROENEWOLD, JAN, CHIU, YU-JEN, KEGEL, WILLEM K, VAN BLAADEREN, ALFONS & ZARZAR, LAUREN D 2020 Predator–prey interactions between droplets driven by non-reciprocal oil exchange. *Nat. Chem.* **12** (12), 1136–1142.
- [50] MICHALET, XAVIER 2010 Mean square displacement analysis of single-particle trajectories with localization error: Brownian motion in an isotropic medium. *Phys. Rev. E* **82** (4), 041914.
- [51] MICHELIN, SÉBASTIEN 2022 Self-propulsion of chemically active droplets. *Annu. Rev. Fluid Mech.* **55**.
- [52] MICHELIN, SÉBASTIEN, LAUGA, ERIC & BARTOLO, DENIS 2013 Spontaneous autophoretic motion of isotropic particles. *Phys. Fluids* **25** (6), 061701.

- [53] MORAN, JEFFREY L & POSNER, JONATHAN D 2017 Phoretic self-propulsion. *Annu. Rev. Fluid Mech.* **49**, 511–540.
- [54] MOROZOV, MATVEY & MICHELIN, SÉBASTIEN 2019 Nonlinear dynamics of a chemically-active drop: From steady to chaotic self-propulsion. *J. Chem. Phys.* **150** (4), 044110.
- [55] MOROZOV, MATVEY & MICHELIN, SÉBASTIEN 2019 Self-propulsion near the onset of marangoni instability of deformable active droplets. *J. Fluid Mech.* **860**, 711–738.
- [56] NAKATA, SATOSHI, KIRISAKA, JUNKO, ARIMA, YOSHIE & ISHII, TOSHIO 2006 Self-motion of a camphanic acid disk on water with different types of surfactants. *J. Phys. Chem. B* **110** (42), 21131–21134.
- [57] NASOURI, BABAK & GOLESTANIAN, RAMIN 2020 Exact axisymmetric interaction of phoretically active Janus particles. *J. Fluid Mech.* **905**.
- [58] NASOURI, BABAK & GOLESTANIAN, RAMIN 2020 Exact phoretic interaction of two chemically active particles. *Phys. Rev. Lett.* **124** (16), 168003.
- [59] PAREDES, PEDRO, HERMANN, MIGUEL, LE CLAINCHE, SOLEDAD & THEOFILIS, VASSILIS 2013 Order 104 speedup in global linear instability analysis using matrix formation. *Comput Methods Appl Mech Eng* **253**, 287–304.
- [60] PAXTON, WALTER F, KISTLER, KEVIN C, OLMEDA, CHRISTINE C, SEN, AYUSMAN, ST. ANGELO, SARAH K, CAO, YANYAN, MALLOUK, THOMAS E, LAMMERT, PAUL E & CRESPI, VINCENT H 2004 Catalytic nanomotors: autonomous movement of striped nanorods. *J. Am. Chem. Soc.* **126** (41), 13424–13431.
- [61] PAXTON, WALTER F, SUNDARARAJAN, SHAKUNTALA, MALLOUK, THOMAS E & SEN, AYUSMAN 2006 Chemical locomotion. *Angew. Chem., Int. Ed. Engl.* **45** (33), 5420–5429.
- [62] PEDDIREDDY, KARTHIK, KUMAR, PRAMODA, THUTUPALLI, SHASHI, HERMINGHAUS, STEPHAN & BAHR, CHRISTIAN 2012 Solubilization of thermotropic liquid crystal compounds in aqueous surfactant solutions. *Langmuir* **28** (34), 12426–12431.
- [63] PENG, GUNNAR G & SCHNITZER, ORY 2022 Weakly nonlinear dynamics of a chemically active particle near the threshold for spontaneous motion. II. history-dependent motion. *arXiv preprint arXiv:2211.09467* .
- [64] PICELLA, FRANCESCO & MICHELIN, SÉBASTIEN 2022 Confined self-propulsion of an isotropic active colloid. *J. Fluid Mech.* **933**.
- [65] POPESCU, MIHAIL NICOLAE, DIETRICH, S, TASINKEVYCH, M & RALSTON, J 2010 Phoretic

- motion of spheroidal particles due to self-generated solute gradients. *Eur. Phys. J. E* **31** (4), 351–367.
- [66] RAO, K JAGAJJANANI, LI, FEI, MENG, LONG, ZHENG, HAIRONG, CAI, FEIYAN & WANG, WEI 2015 A force to be reckoned with: a review of synthetic microswimmers powered by ultrasound. *Small* **11** (24), 2836–2846.
- [67] SCHNITZER, ORY 2022 Weakly nonlinear dynamics of a chemically active particle near the threshold for spontaneous motion: adjoint method. *Phys. Rev. Fluids* .
- [68] SEEMANN, RALF, FLEURY, JEAN-BAPTISTE & MAASS, CORINNA C 2016 Self-propelled droplets. *The European Physical Journal Special Topics* **225** (11), 2227–2240.
- [69] SHARIFI-MOOD, NIMA, MOZAFFARI, ALI & CÓRDOVA-FIGUEROA, UBALDO M 2016 Pair interaction of catalytically active colloids: from assembly to escape. *J. Fluid Mech.* **798**, 910–954.
- [70] SITTI, METIN, CEYLAN, HAKAN, HU, WENQI, GILTINAN, JOSHUA, TURAN, MEHMET, YIM, SEHYUK & DILLER, ERIC 2015 Biomedical applications of untethered mobile milli/microrobots. *P. IEEE* **103** (2), 205–224.
- [71] SOTO, FERNANDO, KARSHALEV, EMIL, ZHANG, FANGYU, ESTEBAN FERNANDEZ DE AVILA, BERTA, NOURHANI, AMIR & WANG, JOSEPH 2021 Smart materials for microrobots. *Chem. Rev.* **122** (5), 5365–5403.
- [72] SUDA, SAORI, SUDA, TOMOHARU, OHMURA, TAKUYA & ICHIKAWA, MASATOSHI 2021 Straight-to-curvilinear motion transition of a swimming droplet caused by the susceptibility to fluctuations. *Phys. Rev. Lett.* **127** (8), 088005.
- [73] SUEMATSU, NOBUHIKO J, IKURA, YUMIHIKO, NAGAYAMA, MASAHARU, KITAHATA, HIROYUKI, KAWAGISHI, NAO, MURAKAMI, MAI & NAKATA, SATOSHI 2010 Mode-switching of the self-motion of a camphor boat depending on the diffusion distance of camphor molecules. *J. Phys. Chem. C* **114** (21), 9876–9882.
- [74] SUEMATSU, NOBUHIKO J, SAIKUSA, KAZUMI, NAGATA, TOSHIKI & IZUMI, SHUNSUKE 2019 Interfacial dynamics in the spontaneous motion of an aqueous droplet. *Langmuir* **35** (35), 11601–11607.
- [75] SUGA, MARIKO, SUDA, SAORI, ICHIKAWA, MASATOSHI & KIMURA, YASUYUKI 2018 Self-propelled motion switching in nematic liquid crystal droplets in aqueous surfactant solutions. *Phys. Rev. E* **97** (6), 062703.

- [76] TANG, SONGSONG, ZHANG, FANGYU, GONG, HUA, WEI, FANAN, ZHUANG, JIA, KARSHALEV, EMIL, ESTEBAN-FERNÁNDEZ DE ÁVILA, BERTA, HUANG, CHUYING, ZHOU, ZHIDONG, LI, ZHENGXING & OTHERS 2020 Enzyme-powered janus platelet cell robots for active and targeted drug delivery. *Sci. Robot.* **5** (43), eaba6137.
- [77] THUTUPALLI, SHASHI, GEYER, DELPHINE, SINGH, RAJESH, ADHIKARI, RONOJOY & STONE, HOWARD A 2018 Flow-induced phase separation of active particles is controlled by boundary conditions. *Proc. Natl. Acad. Sci. USA* **115** (21), 5403–5408.
- [78] THUTUPALLI, SHASHI & HERMINGHAUS, STEPHAN 2013 Tuning active emulsion dynamics via surfactants and topology. *Eur. Phys. J. E* **36** (8), 1–10.
- [79] TOMLINSON, CHARLES, II. 1862 On the motions of camphor on the surface of water. *Proc. Roy. Soc. London* (11), 575–577.
- [80] VYSKOCIL, JAN, MAYORGA-MARTINEZ, CARMEN C, JABLONSKA, EVA, NOVOTNY, FILIP, RUMML, TOMAS & PUMERA, MARTIN 2020 Cancer cells microsurgery via asymmetric bent surface au/ag/ni microrobotic scalpels through a transversal rotating magnetic field. *ACS Nano* **14** (7), 8247–8256.
- [81] WENTWORTH, CIERA M, CASTONGUAY, ALEXANDER C, MOERMAN, PEPIJN G, MEREDITH, CALEB H, BALAJ, REBECCA V, CHEON, SEONG IK & ZARZAR, LAUREN D 2022 Chemically tuning attractive and repulsive interactions between solubilizing oil droplets. *Angew. Chem., Int. Ed. Engl.* **61** (32), e202204510.
- [82] YANG, QIANHONG, JIANG, MAOQIANG, PICANO, FRANCESCO, JIN, CHENYU & LAILAI, ZHU 2023 Collective behaviors of isotropic phoretic microswimmers: from crystalline solids to active turbulence. *arXiv preprint arXiv:2304.01593* .
- [83] YARIV, EHUD & KAYNAN, URI 2017 Phoretic drag reduction of chemically active homogeneous spheres under force fields and shear flows. *Phys. Rev. Fluids* **2** (1), 012201.